Journal of Thermal Analysis and Calorimetry (2019) 137:1827–1840
https://doi.org/10.1007/s10973-019-08057-3

Mineralogical and chemical investigation of Tunisian phosphate washing waste during calcination

R. Dabbebi[1,2] · J. L. Barroso de Aguiar[2] · B. Samet[1] · S. Baklouti[1]

Received: 1 September 2018 / Accepted: 31 January 2019 / Published online: 20 February 2019

Abstract

Phosphate washing waste (PWW) is one of the wastes generated by the phosphate mine with a very high amount. This waste was investigated in this work to study the effect of the calcination of the PWW at four different temperatures 600 °C, 700 °C, 800 °C and 900 °C on its mineralogical and chemical composition. The samples were investigated by X-ray powder diffraction, Fourier transform infrared, differential scanning calorimetry and thermogravimetric analysis, solid-state magic angle spinning nuclear magnetic resonance of ^{29}Si, ^{27}Al and ^{31}P and scanning electron microscope. The results show that the PWW presents a complex system and it suffers a significant change on its mineralogical and chemical composition after calcination. It reveals the presence of carbonate, natural zeolite, fluorapatite, quartz and clay. After calcination, the waste shows the disappearance of some of these phases and the appearance of others and some other phases remain steady.

Keywords Phosphate washing waste · Calcination · Mineralogy · XRD · DSC–TG · FTIR · MAS-NMR

Abbreviations

CPG	Gafsa Phosphate Company
XRD	X-ray powder diffraction
DSC–TG	Differential scanning calorimetry and thermogravimetric analysis
FTIR	Fourier transform infrared
ATR	Attenuated total reflectance
MAS-NMR	Magic angle spinning nuclear magnetic resonance
PWW	Phosphate washing waste
SEM	Scanning electron microscope

Introduction

Phosphate rock ore is one of the principal minerals produced in the world. Based on industry analysts, the production of this ore attains about 147 million ton in 2017 and it can increase to achieve 168 million ton in 2021 [1]. This ore was used as raw material for the production of phosphate fertilizers used in the agricultural sector, chemical and detergents industries [2–4]. The principle producers in the world are China, USA, Morocco, Russia and Tunisia [1, 2, 5]. In Tunisia, the phosphate deposits that take place in height opencast mines in Radayef, Moularaés, Metlaoui and Mdhilla [6] for more than a century are operated by the Gafsa Phosphate Company CPG. It extracts more than 8 million ton of natural phosphate yearly [6, 7]. These phosphate deposits are sedimentary which did not contain crystalline apatite, but are formed mainly of cryptocrystalline phosphate minerals [8]. Many authors [9–12] reported the chemical composition of the Tunisian phosphate ore, which indicates that the major oxides are CaO, P_2O_5 and others with minor quantities such as SiO_2, Na_2O and SO_3. According to [8–10, 13, 14], the phosphate ore has the carbonate-fluorapatite, calcite and dolomite as predominantly mineralogical phases and others like quartz and gypsum. In the process of the enrichment of the phosphate, it is washed with flocculant, including mechanical separation and treatment to eliminate the barren components [12, 13] and it is sorted in three categories depending on its grain size, gros particles > 2 mm, 80 µm $<$ phosphorite < 2 mm and phosphate sludge < 80 µm. The intense production of the natural phosphate engenders a huge amount of waste [6, 15, 16].

✉ R. Dabbebi
Dabbebirawia@gmail.com

[1] Laboratory of Industrial Chemistry, University of Sfax, 3038 Sfax, Tunisia

[2] C-TAC Research Centre, University of Minho, 4800-058 Guimarães, Portugal

This waste can be divided into three different types: The waste rock, the phosphogypsum and phosphate sludge also named as tailing and phosphate slime [17, 18].

Discussing the case of the phosphate sludge, this waste was generating with quantity about 1 ton for the production of 1 ton of phosphate [2, 6, 16–18] which is deposited in large pond and causes a serious problem to the environment. Therefore, the phosphate sludge has been a question in the latest 10 years of great interest in a wide range of fields: to control acid mine drainage [17], in ceramic [4, 17, 19, 20], as aggregate [17, 21, 22], as a natural absorbent for phosphorous removal from aqueous solutions [15, 16, 23], as a membrane [24, 25] and as a precursor for geopolymeric materials [26, 27].

A number of studies [22, 23, 27, 28] have investigated the composition of the phosphate sludge which is composed essentially of carbonate (calcite, dolomite), clay, quartz and fluorapatite. Most of these researchers investigated the phosphate sludge as a raw material in different areas, without any treatment. It should be mentioned that the phosphate sludge has a high content of clay [18] and since the calcination is a mandatory step in the use of clay like kaolinite and illite to attend its best reactivity and performance [29, 30], the calcination can also have an effect on the phosphate sludge phases. However, data about the effect of the calcination on the present phases on the phosphate sludge are limited.

Therefore, this paper set out to assess the effect of the calcination at different temperatures on the present phases in the phosphate washing waste. The comprehension of the behavior of the Tunisian phosphate washing waste after thermal treatment from 25 to 900 °C shows that this material can be valorized in ceramic geopolymer and zeolite.

Materials and methods

The phosphate washing waste PWW used in this investigation was obtained from the storage ponds of Metlaoui Tunisia (Laverie IV). The waste was filtered and dried at 105 °C for 24 h. It was crushed and then sieved to the grain size less than 100 µm.

The obtained powder was calcined at four different temperatures 600 °C, 700 °C, 800 °C and 900 °C for 2 h with heating rate 10 °C min^{-1} from room temperature to the required temperatures. The calcination was performed in a muffle furnace LABTECH Daihan LABTech Co., Ltd, and then the samples were studied with XRD, FTIR, MAS-NMR and SEM techniques.

Experimental

The phase identification of the samples was performed by powder X-ray diffraction XRD Bruker D_8 Discover using Cu Kα radiation λ = 1.54060 Å at 40 kV and 40 mA in the range from 5° to 60° with a step width of 0.02°. Phase identification was done using X'Pert Highscore software.

The thermal analysis DSC–TG was performed under argon atmosphere with heating rate 10 °C min^{-1} from ambient to 1000 °C with TA instruments SDT 2960 Simultaneous for a quantity of PWW = 31.2867 mg

An attenuated total reflectance (ATR) FTIR spectra were scanned from 400 to 4000 cm^{-1} wavenumbers using the Fourier transform infrared model PerkinElmer spectrum BX spectrometer, and spectra were collected for four scans at a resolution 2 cm^{-1}. No special preparation of the samples was required.

The solid-state magic angle spinning nuclear magnetic resonance MAS-NMR of the samples was made using high-resolution Bruker AMX 300 spectrometer equipped with $B_0$7.1T super-induction magnetic.

The ^{29}Si spectra were operating at a frequency 59.63 MHz and spun at 8 kHz. The chemical shift is reported in parts per million (ppm) relative to tetramethylsilane TMS.

The ^{27}Al spectra were operating at a frequency 78.21 MHz and spun at 8 kHz. The chemical shifts are reported referring to $AlCl_3{\cdot}6H_2O$.

The ^{31}P spectra were operating at a frequency 121.49 MHz and spun at 8 kHz. The chemical shift is reported referring to fluorapatite.

For the analysis of the microstructure, the samples were executed using a scanning electron microscope SEM 200 operating at 15 kv. Before analysis, the samples were sputter coated with 40-nm film of Au–Pd (80–20 mass%).

Results and discussion

Chemical composition and particle size

As mentioned in the previous work [26], the phosphate washing waste presents an important amount of silica SiO_2 42%, calcium CaO 25.5%, phosporous P_2O_5 10% and alumina Al_2O_3 9.77%. The PWW was characterized by a major population of grain size equals to 7.5 µm and a less dominant population with a particle size equals to 100 µm.

Based on the results of the chemical composition of previous work of Elgharbi S, et al et Galai H, et al of the Tunisian phosphate ore presented in Table 1 and the chemical composition of the phosphate washing waste, it shows that the main oxides of each material are not the

Table 1 Chemical composition of PWW and phosphate ore in oxide mass%

	P_2O_5	CaO	SiO_2	Al_2O_3	Na_2O	K_2O	MgO	Fe_2O_3	F_2O	SO_3	Refs.
PWW	10	26.5	42	9.77	1.12	0.673	3.09	2.31	0.96	3.39	[26]
$Phosphate_1$	29.58	49.45	3.08	0.86	1.39	0.054	0.7	0.25	2.84	3.58	[11]
$Phosphate_2$	25.88–29.51	43.56–47.25	2.25–8.66	0.07–0.41	1.47–1.66	0.05–0.16	0.47–0.62	0.18–0.30	–	1.85–3.45	[12]

same. The phosphate ore has the P_2O_5 and CaO as main oxides, while the PWW has the SiO_2 and the CaO as main oxides. These results explain also the difference of the present minerals in the both materials.

XRD characterization

The X-ray diffractograms of the non-calcined and calcined PWW are shown in Fig. 1. The patterns show the mineralogical constituents of the samples at different temperatures. The main mineral components in the sample at 25 °C are: the potassic-heulandite with strong reflections at 8.77 Å, 7.76 Å and 3.92 Å. Based on different study of the Tunisian phosphate ore [10, 12], the clinoptilolite was presented as the main natural zeolite in the ore. Other works [8, 31] present the heulandite as the principle natural zeolite. The Heu zeolite-type "heulandite-clinoptilolite" was difficult to differentiate between them, while they react upon heating with different ways depending on their structural properties [32, 33]. In this investigation, the heulandite is presented as the natural zeolite because its reflection starts to decrease from 600 °C until it disappears after thermal treatment but the clinoptilolite retains its state after calcination [32]. The palygorskite is presented with reflection at 10.13 Å, 6.34 Å and 4.41 Å. The pattern shows also the presence of calcite which is confirmed by

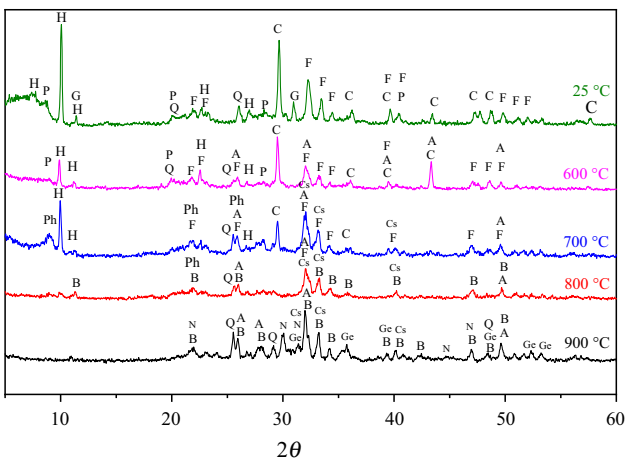

Fig. 1 X-ray diffractograms of the PWW at 25 °C, 600 °C, 700 °C, 800 °C and 900 °C. C: calcite, F: carbonate-fluorapatite, P: palygorskite, H: heualandite, Q: quartz, G: gypsum, A: anhydrite, Ph: phlogopite, B:fluorapatite, Cs: C_2S, Ge: gehlenite, N: anortithe

the chemical composition and the thermal analysis discussed later. It presents a reflection at 3.01 Å, 2.48 Å and 2.27 Å. The diffractogram shows also the presence of carbonate-fluorapatite 2.77 Å, 2.67 Å and 2.60 Å, and it shows also the presence of the quartz characterized by the reflection at 4.41 Å, 3.42 Å and the gypsum by the reflection at 7.76 Å, 2.88 Å and 2.67 Å. As we can see, after calcination, the pattern shows the appearance of some phases and disappearance of the others. The carbonate-fluorapatite becomes fluorapatite at 800 °C [11], it remains unchanged with quartz also until 900 °C, and this is explained that these phases were not affected by the thermal treatment [22]. The intensity of the reflections of the heulandite and the calcite decreases at 600 °C and 700 °C until they disappear at 800 °C. This can be explained by the contraction of the volume of the heulandite until the destruction of the structure [32]. The decomposition of calcite can clarify the decrease in its intensity [34].

The reflection of palygorskite drops at 600 °C. This is caused by the dehydration and deformation of the structure. It vanished at 700 °C, and this can be explained by the complete dehydroxylation of the palygorskite [35].

The reflections of the gypsum (calcium sulfate dihydrate $CaSO_4{\cdot}2H_2O$) disappear at 600 °C because the gypsum with the increasing of temperature starts to dehydrate until a total dehydration; thereafter, it forms anhydrite as presented in Eq. 1. The presence of the anhydrite was confirmed by its reflections that appear in the sample calcined at 700 °C.

$$CaSO_4 \cdot 2H_2O \overset{\text{Temperature °C}}{\rightarrow} CaSO_4 + 2H_2O_{(g)} \quad (1)$$

The phlogopite which can be represented by the formula $KMg_3AlSi_3O_{10}(OH)_2$ [36] appears at 700 °C with reflection at 9.88 Å, 4.05 Å and 3.43 Å, and it remains at 800 °C. The presence of this phase results from the decomposition of palygorskite and the alteration of the structure of the potassic-heulandite [37].

The curves display also the appearance of Ca_2SiO_4 (C_2S) at 700 °C, 800 °C and 900 °C with a reflection at 2.79 Å, 2.69 Å and 2.24 Å. The pattern of the sample calcined at 900 °C shows the appearance of two new phases, gehlenite $Ca_2SiAl_2O_7$ (C_2AS) with fundamental reflections at 2.85 Å, 2.28 Å and 1.74 Å and anorthite $CaAl_2Si_2O_8$ at (CAS_2) with reflections at 3.19 Å, 2.50 Å and 2.13 Å which are formed from the free lime from the

decarbonation of the calcite and the decomposition of the heulandite and phlogopite [38, 39]. The main d-values of the present phases at the different temperature are displayed in Table 2.

DSC–TG

The results obtained from the thermal behavior of the PWW Fig. 2 are presented in the previous work [26]. The TG curve shows three mass losses, respectively, from 30 to 140 °C, from 200 °C to 500 °C and from 650 °C to 770 °C with a total mass loss approximately 17%. The removal of the adsorbed water results in the first endothermic peak and the first mass loss ∼ 2.35%. The release of adsorbed zeolitic water localized in the cavities and channels of the potassic-heulandite without the decomposition of the structure [40] and the zeolitic water of palygorskite [41] leads to the second endothermic peak and to the second mass loss ∼ 4.69%, considering also in this gap of temperature the combustion of the organic matter defined by an exothermic peak at around 550 °C. The decomposition of the calcium carbonate $CaCO_3$ during the heating with the release of the $CO_{2(g)}$ reveals an endothermic peak and a third mass loss ∼ 9.96%. The obtained results are in good agreement with the XRD results.

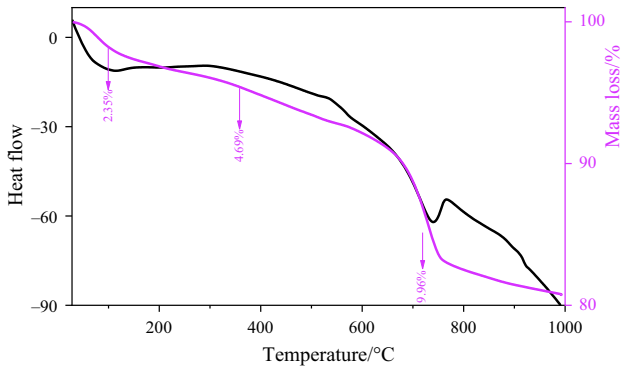

Fig. 2 DSC–TG of phosphate washing waste

FTIR characterization

The IR spectra of the samples are presented in Fig. 3. This figure shows that the calcination process had a remarkable

Table 2 Summarization of the present phases at different temperatures

	d-spacing/Å				
	25 °C	600 °C	700 °C	800 °C	900 °C
Carbonate-fluorapatite 00-002-0833	2.77–2.67–2.61	2.77–2.66–2.62	2.79–2.69–2.62	–	–
Fluorapatite 00-002-0845	–	–	–	2.79–2.69–2.61	2.79–2.69–2.61
Calcite 00-002-0629	3.01–2.48–2.27	3.02–2.48–2.27	3.02–2.49	–	–
Heulandite k 01-076-2214	8.86–7.93–3.92	8.98–7.88–3.94	8.88–7.82–3.49	–	–
Palygorskite 00-029-0855	10.13–6.34–4.41	10.21–4.44	–	–	–
Gypsum 00-021-0816	7.76–2.88–2.67	–	–	–	–
Quartz 01-070-2535	4.41–3.42	4.44–3.43	3.43	3.43	3.43
Anhydrite 00-003-0368	–	3.4–2.79–1.38	3.49–2.79–1.83	3.47–2.79–1.83	3.48–2.79–1.83
C_2S 00-023-1042	–	–	2.81–2.71–2.22	2.81–2.69–2.24	2.85–2.69–2.24
Phlogopite 01-079-2364	–	–	9.85–4.02–3.41	2.69	–
Gehlenite 00-001-0982	–	–	–	–	2.85–2.28–1.74
Anorthite 00-002-0523	–	–	–	–	3.19–2.50–2.13

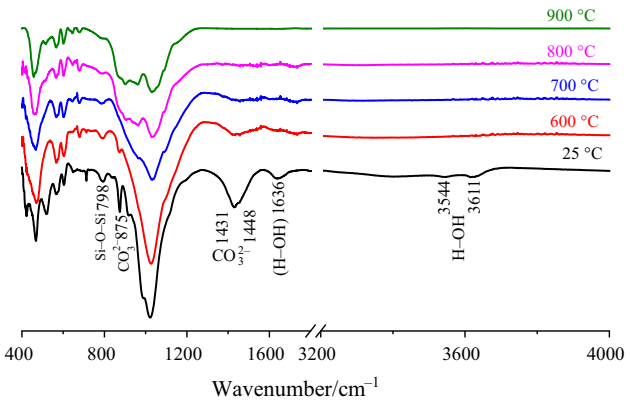

Fig. 3 FTIR of PWW at 25 °C, 600 °C, 700 °C, 800 °C and 900 °C

effect on the vibrational bands intensity and its positions and on the appearance and disappearance of some bands. In general, Fig. 3 shows that the spectra had a sensitive region to the calcination process between 400 and 1200 cm^{-1}. It can generally be stated that the interpretation of the FTIR bands even with deconvoluted spectra may be difficult because of the multiphase system, bond vibration of various phases with similar or approximately the same wavenumber value which can be jointly overlapped or summed together.

The sensitive region can be decomposed into two regions: 400–800 cm^{-1} (Fig. 4) and 800–1200 cm^{-1} (Fig. 5).The latest region was deconvoluted and indicates that the most interesting aspect is that with the increase in the calcination temperature, the absorption band is broadened out and its intensity decreases. This phenomenon can be explained by the increase in structural disorder in the lattice [42].

Comparing the FTIR spectra of the PWW at ambient temperature with the FTIR presented in [8, 11, 12] of the phosphate ore, it was noticeable that the main and strong band was of the PO_4^{3-} and CO_3^{2-}. While, the PWW shows that the main band is for the Si–O–T with T: Si or Al. The

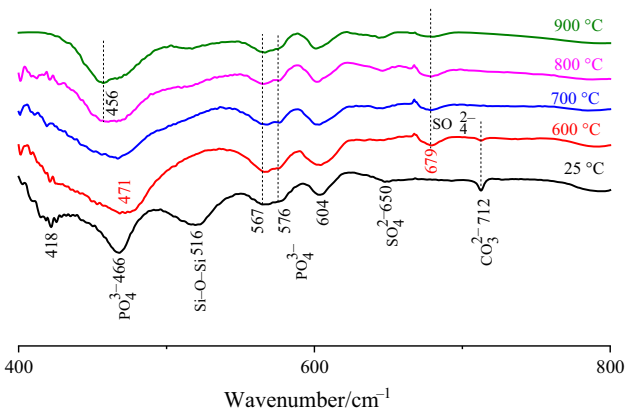

Fig. 4 FTIR of PWW at different temperatures from 400 to 800 cm^{-1}

investigation of Elagharbi et al. [11] with FTIR of the phosphate ore is calcined at different temperatures. The main band of PO_4^{3-} at about 1049 cm^{-1} becomes narrower and more distinguishable after thermal treatment. In contrary, for the PWW investigated at different temperatures, the curves show that the temperature changes the intensity and the width of the main bands.

The spectrum in Fig. 3 of the PWW at 25 °C shows bands at around 3544 and 3611 cm^{-1} assigned to the stretching vibration mode of H–OH group and a band at around 1636 cm^{-1} corresponding to the bending vibration modes of H–OH which is due to the adsorbed water. These two bands disappear after calcination from 600 to 900 °C.

The presence of carbonate-fluorapatite in the PWW can be confirmed by the vibration band of phosphate group PO_4^{3-} at 466 cm^{-1} which corresponds to the v_2 symmetric bending mode. The asymmetric v_4 mode gives three main bands 567, 576 and 604 cm^{-1}. The spectrum at 25 °C shows a band at 966 cm^{-1} corresponding to the v_1 mode and v_3 mode at 1050 cm^{-1}. After calcination, the FTIR spectra show that some of the characteristic bands of PO_4^{3-} group made a slight shift and they appear at 601 and 962 cm^{-1}. The shoulder at 1100 cm^{-1} which appears after calcination at 700 °C corresponds to the v_3 mode of PO_4^{3-} group [34, 43].

The FTIR at 25 °C displays also the presence of calcite by the detection of the carbonates group. The characteristic bands were the v_2 out-of-plane bending of CO_3^{2-} group corresponding to the band at 712 cm^{-1}. The v_4 splits in-plane bending vibration of CO_3^{2-} at 875 cm^{-1}, and the last band at 1431 cm^{-1} corresponds to the asymmetric stretch v_3 [44, 45]. After calcination, these bands persist at 600 and 700 °C but with lower intensity and they vanished totally at 800 and 900 °C.

In this spectrum, it is possible to identify the gypsum with the band at 650 cm^{-1} which corresponds to the in-plane bending vibrational mode v_4 of SO_4^{2-}. 1120 and 1150 cm^{-1} are assigned to the asymmetric stretching vibrational mode v_3, and the symmetric stretching vibrational mode v_1 at 1000 cm^{-1} [46]. After calcination, the band at 650 cm^{-1} made a shift to higher frequency 697 cm^{-1} at 600, 700, 800 and 900 °C which is a characteristic of the anhydrite. This shift was because of the less water in the structure because generally the hydrogen bending in the structure of gypsum diminishes the frequency of the absorption band. The same bands of the SO_4^{2-} group appear at the calcination temperature at 1120 and 1150 cm^{-1} [47].

The presence of palygorskite in the matrix of the PWW can be identified by the band at approximately 520 cm^{-1} attributed to the silicate tetrahedral sheet deformation Si–O–Si bending vibration. Furthermore, other bands can be

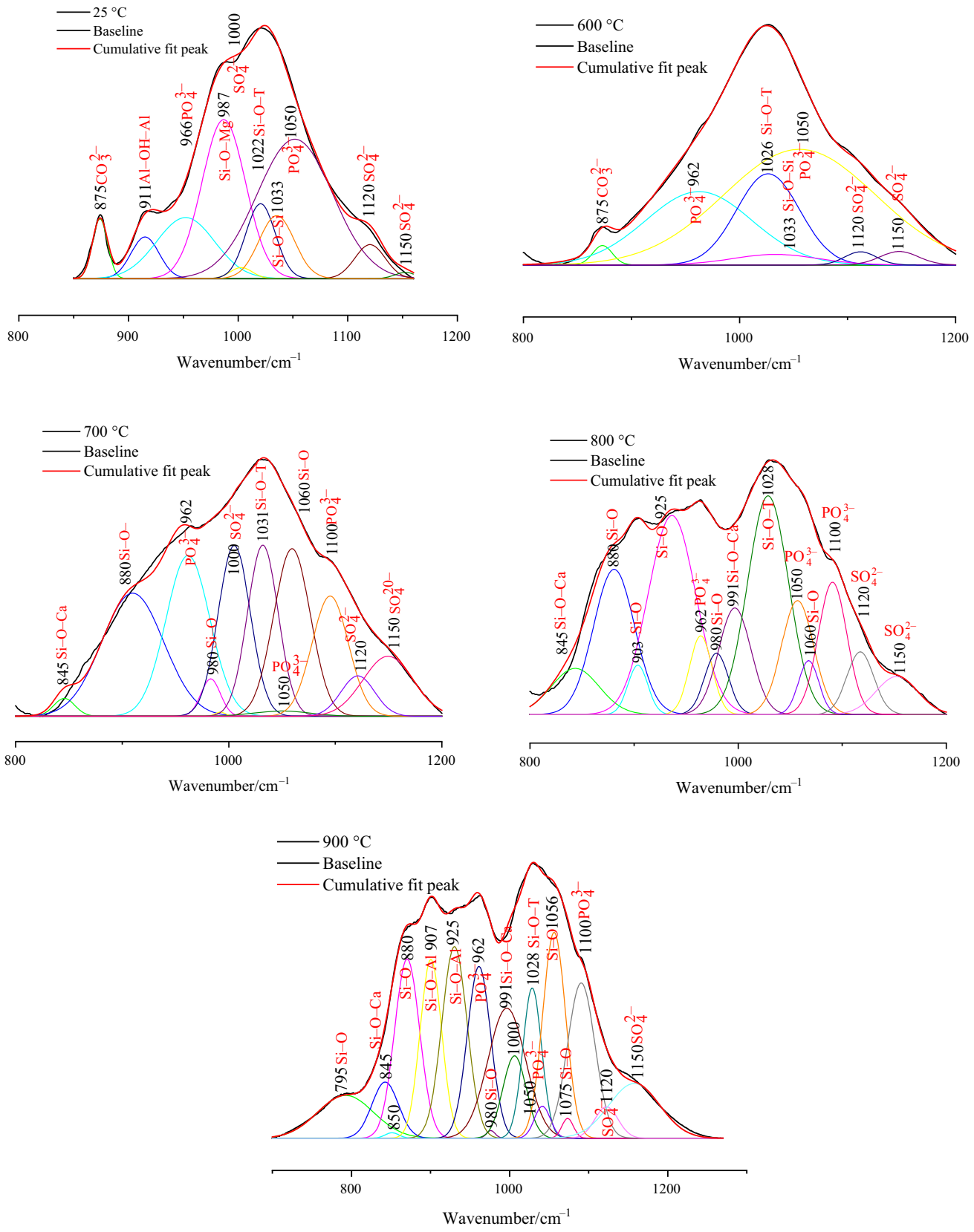

Fig. 5 Deconvolution of the spectra of PWW at different temperatures from 800 to 1200 cm^{-1}

Table 3 ATR–FTIR band assignment

Assignment	Wavenumber/cm^{-1}				
	25 °C	600 °C	700 °C	800 °C	900 °C
Carbonate-fluorapatite					
PO_4^{3-}	466–567–576–604–944–1050	604–962–1050	601–962–1100	–	–
CO_3^{2-}	1448	1448			
Fluorapatite					
PO_4^{3-}	–	–	–	601–962–1100	601–962–1100
Calcite					
CO_3^{2-}	712–875–1431	712–875–1431	712–1431	–	–
Heulandite K					
Si–O–Si	1022	1026	1031	–	–
Si–O–Al					
Palygorskite					
Si–O–Si	520		–	–	–
Al–OH–Al	911				
Si–O–Mg	987	987			
Si–O–Si	1033	1033			
Gypsum					
SO_4^{2-}	650–1120–1150	–	–	–	–
Quartz					
Si–O–Si	798	798	798	798	798
Anhydrite					
SO_4^{2-}	–	697–1120–1150	697–1120–1150	697–1120–1150	697–1120–1150
C2S					
Si–O	–	–	512–880	512–880	512–880
Si–O–Ca			845–991	845–991	845–991
Phlogopite					
Si–O	–	–	980–1060	980	
Gehlenite					
Al–O–Al, $Si(Al_4)(O_3)$	–	–	–	–	907–925–1056–850
Anorthite					
AlO_4, SiO_4	–	–	–	–	1075–1135

detected at 25 °C FTIR as the band at 911 cm^{-1} which is assigned to the bending vibration of the octahedral Al–OH–Al, the 987 cm^{-1} band attributed to the perpendicular Si–nonbridging oxygen–Mg (Si–O_{nb}–Mg) asymmetric stretching vibration [35] and a band at 1033 cm^{-1} corresponding to the asymmetric stretching vibration Si–O–Si. After calcination at 600 °C, the bands at 520 cm^{-1} and at 911 cm^{-1} disappear through the destruction of the structure and the dihydroxylation of Al–O–Al, respectively [35, 48].

As mentioned in the section of XRD of the PWW, the potassic-heulandite is distinguished in the FTIR at 25 °C via a band at 1022 cm^{-1} assigned to the asymmetric stretching mode of Si–O–Si and Si–O–Al [32, 49]. This band shifts to the higher frequency 1026 cm^{-1} and 1031 cm^{-1} at 600 °C and 700 °C, respectively. This shift can be explained by the Si/Al molar ratio in the structure of heulandite, and the vibration mode shifts to higher frequency when the number of tetrahedral Al atoms decreases [40].

At 700 °C, the PWW reveals the C_2S and phlogopite as new phases, and they can be recognized in the FTIR curve at 700 °C. The phlogopite can be identified by the bands at 980 cm^{-1} assigned to the –Si–O vibration and 1060 cm^{-1} assigned to the Si–O vibration in the amorphous SiO_2 [50].

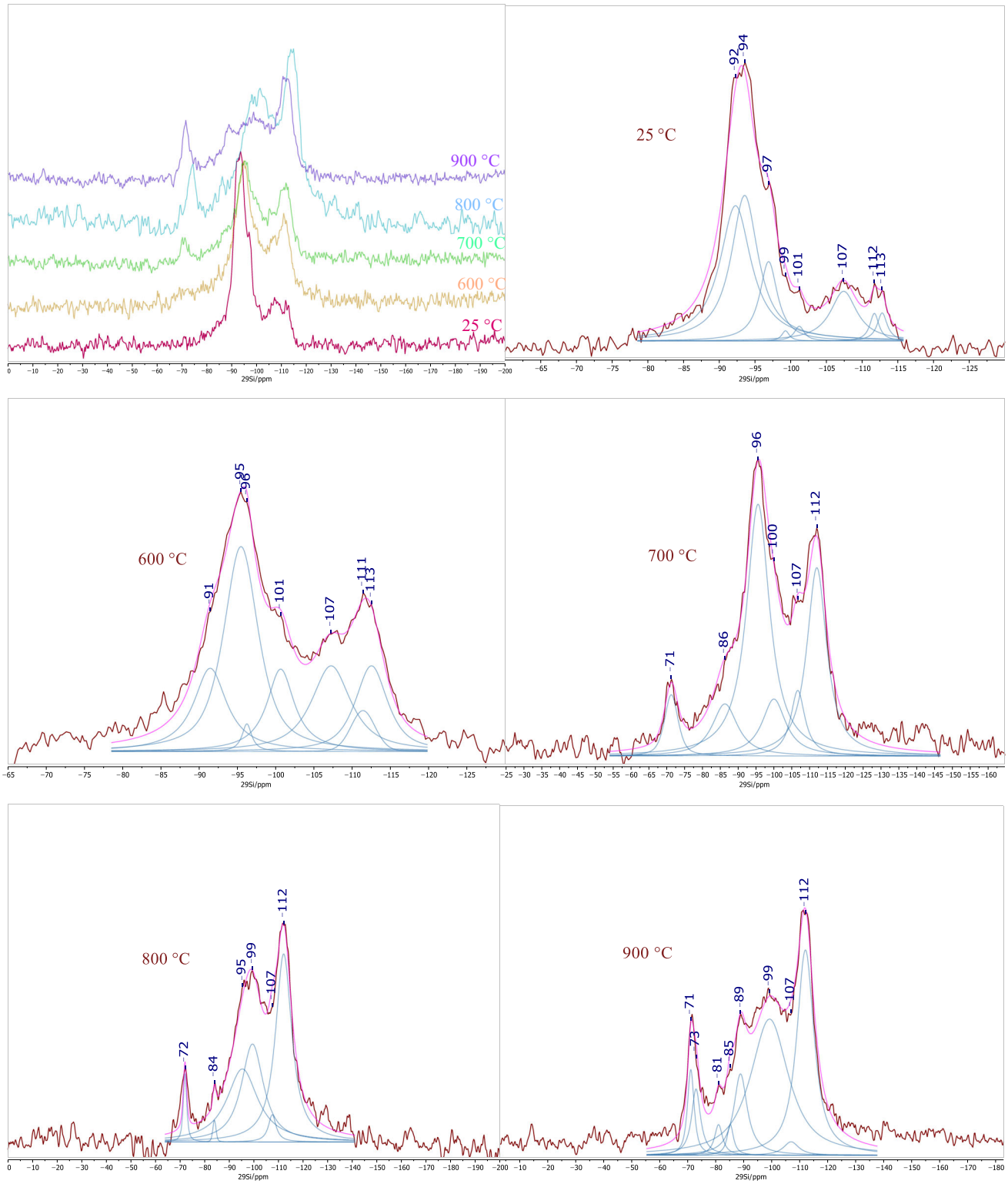

Fig. 6 ^{29}Si MAS-NMR spectra of PWW at 25 °C, 600 °C, 700 °C, 800 °C and 900 °C

The C_2S phase shows a first weak band at 700 °C at 512 cm^{-1} which corresponds to Si–O out-of-plane bending mode, and this band becomes clearer at 800 °C and 900 °C. The C_2S has also other characteristic bands at 880 cm^{-1} corresponding to asymmetric stretching vibration of Si–O, and the bands at 845 cm^{-1} and 991 cm^{-1} correspond to symmetric stretching vibration mode of Si–O–Ca [51–53]. It should be mentioned that the phlogopite remains at 800 °C,

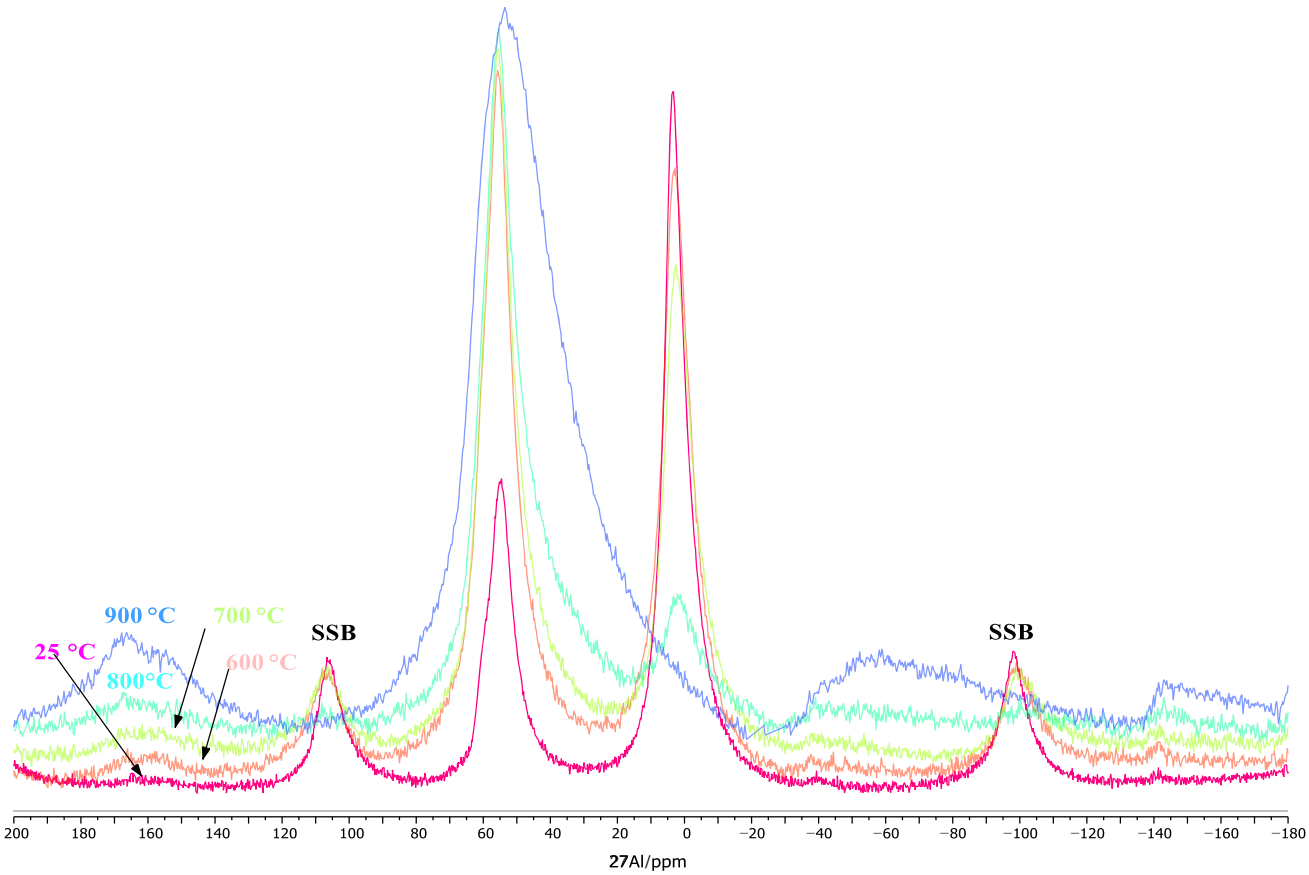

Fig. 7 ^{27}Al MAS-NMR spectra of PWW at 25 °C, 600 °C, 700 °C, 800 °C and 900 °C

but it disappears at 900 °C and at this temperature appears two more new phases as discussed in the XRD section, because the calcination at a temperature higher than 800 °C favors the crystallization of Ca–Al silicate minerals such as gehlenite and anorthite [54]. The anorthite was characterized by three bands at 980 cm^{-1}, 1075 cm^{-1} and 1135 cm^{-1} assigned to asymmetric stretching vibrations of both SiO_4 and AlO_4 tetrahedra [55, 56].The gehlenite was characterized by the bands which confirm the structure at 907 cm^{-1} and 1056 cm^{-1} and the bands at 925 cm^{-1} and 850 cm^{-1} related to the asymmetric stretching of (Si, Al)(O_3) and Al–O–Al, respectively [54].

The band at approximately 798 cm^{-1} has been described as the Si–O–Si symmetric stretching vibration of quartz, and the intensity of the band made a slight change indicating that the Si–O–Si structure was partially destroyed. Table 3 summarized the functional groups of the phases present in each temperature.

MAS-NMR characterization

Considering the composition of the PWW which contains essentially aluminosilicates and zeolite, a study by the ^{29}Si and ^{27}Al solid-state NMR spectroscopy can be interesting. As mentioned in the literature review, the SiO_4 can take place in isolated or combined structure [57, 58]. A strong relationship between the polymerization degree of the silicate polyhedral and the chemical shift is explained in terms of various Q^n environment of silicon, where n is the number of coordinated oxygens that bridge to other silicon.

Generally, the ^{29}Si MAS-NMR of the PWW in function of temperature reveals a significant change in the intensity of the Q^n units peaks. Increasing the temperature, the Q^3 site decreases which implies the dehydration and the decomposition of some phases. Meanwhile, the increase in the Q^0 and Q^4 sites can be assigned to the formation of new phases. The patterns of the ^{29}Si present in Fig. 6 at the 25 °C palygorskite exhibit two peaks at − 92 and − 97 ppm attributed to Q^3 (mAl) [59]. These peaks shifted toward 91 and 96 ppm at 600 °C with a lower intensity.

The heulandite was characterized by peaks at 93 due to Q^4(2Al), − 99 and − 101.20 ppm due to Q^4(1Al). These peaks appear also at 600 °C and 700 °C at (− 95 and 101 ppm) and (95 and 100 ppm), respectively [57, 60].The chemical shift at about − 107 ppm was attributed to the quartz phase present in the PWW which corresponds to unsubstituted units Q^4(0Al). At 700 °C, the 29Si MAS-NMR shows the appearance of two new peaks at − 71 and

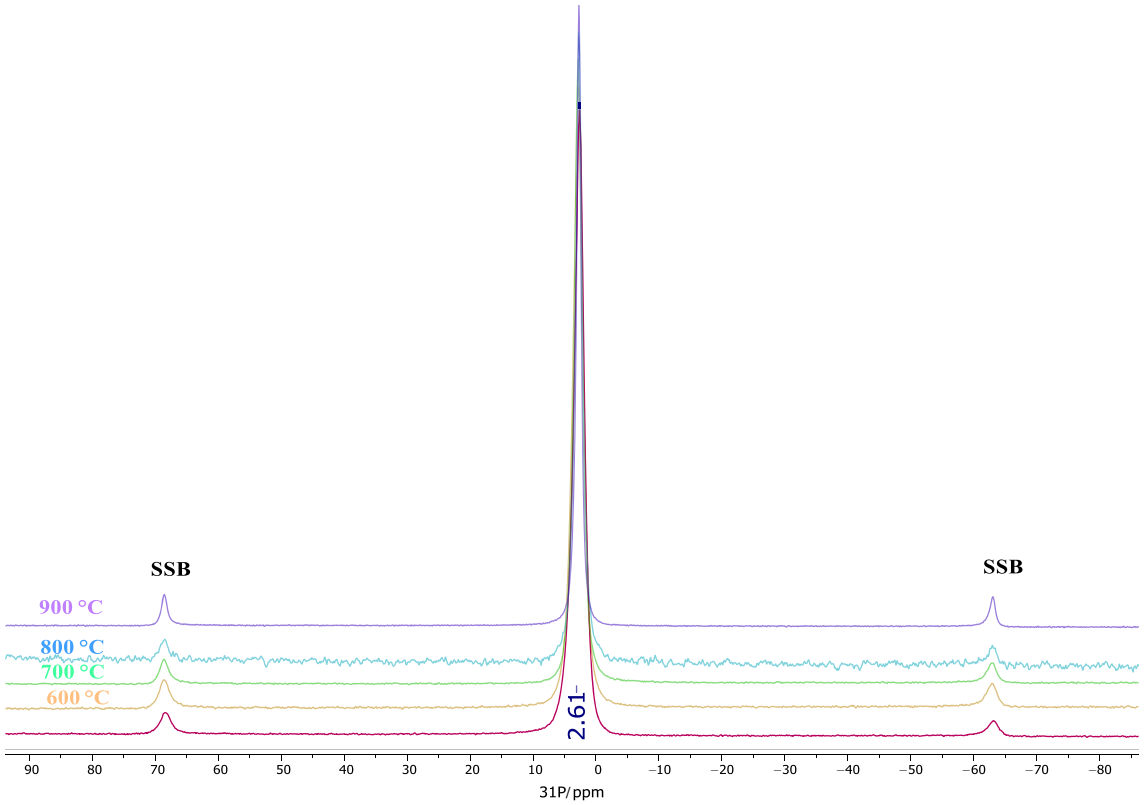

Fig. 8 ^{31}P MAS-NMR of PWW at 25 °C, 600 °C, 700 °C, 800 °C and 900 °C

− 86 ppm. The presence of the phlogopite phase at the PWW calcined at 700 °C was confirmed by the peak at − 86, and it became − 84 at 800 °C which results from the different Si environment Q^3(1Al) and Q^3(2Al), respectively [37]. The C_2S appears at 700 °C, 800 °C and 900 °C, and it was characterized by a single narrow signal at about − 71 ppm assigned to Q^0 unit [61, 62]. At 900 °C and as it is mentioned in the XRD results, the calcined PWW shows the appearance of two new phases, gehlenite characterized by a peak at − 73 ppm which corresponds to Q^1 unit [63, 64] and the anorthite phase defined by − 84, − 89 and − 93 ppm assigned to Q^4(mAl) [65, 66]. The ^{29} Si results show also that the peak at − 111 and − 112 ppm becomes more intense after calcination process which indicate the presence of framework with no bonded Al Q^4(0Al) units.

If we now turn to the ^{27}Al results, according to many researchers [57, 67], the 4-coordinated Al occurring at about 50–80 ppm and the 6-coordinated occurring at about − 10 to 15 ppm and the 5-coordinated Al in well-defined crystalline compounds exhibit a chemical shift at about 30–40 ppm. From Fig. 7, it is apparent that the calcined and uncalcined PWWs show two significant Al sites, 4-coordinated noted ^{IV}Al and 6-coordinated noted ^{VI}Al which change of the intensity by the increase in the calcination temperature. Considering the structure of the palygorskite phase, the coordination of Al is mainly octahedral, which is placed in the center of the octahedral sheet in the layer structure, appearing at 25 °C with a peak at approximately 3 ppm. After calcination at 600 °C, the intensity of the peak decreases following the dehydroxylation of the Al $(O, OH)_6$ octahedra [68]. It shows also a small peak at about 54 ppm corresponding to the ^{IV}Al present in the structure of palygorskite.

The ^{27}Al MAS-NMR exhibits a peak at about 58.03 ppm due to the 4-coordinated Al present in the heulandite framework [69]. After calcination at 600 °C, the intensity of 6-coordinated Al decreases although the intensity of the 4-coordinated Al increases and this is explained by the dehydroxylation of the Al $(O, OH)_6$ which generates a 4-coordinated Al. At 700 °C, the peak at about 2 ppm decreases and the peak at 56 ppm remains steady, which is a character of the phlogopite phase [37]. The presence of the 6-coordinated Al can be defined by the presence of Al in extra framework and also by the ^{VI}Al substitution of Mg. At 800 °C, the peak of ^{VI}Al made an important drop and presented a chemical shift equal to 1 ppm which is the result of the total dehydroxylation of the 6-coordinated Al. The ^{IV}Al becomes broader for the

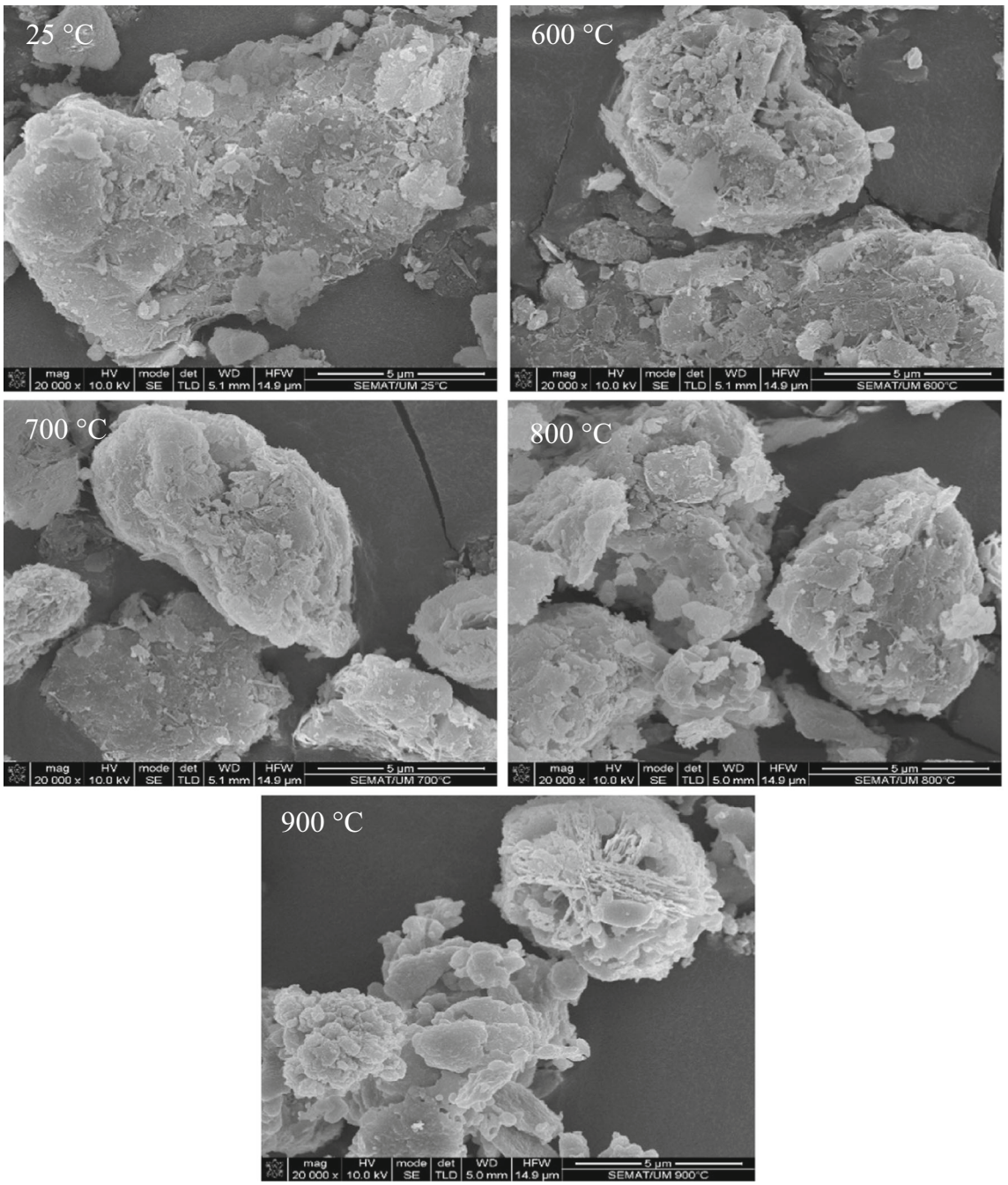

Fig. 9 SEM of PWW at 25 °C, 600 °C, 700 °C, 800 °C and 900 °C

PWW calcined at 900 °C with a maximum at 53 ppm which confirms that most of the Al are in tetrahedral environment and confirms also the presence of gehlenite [65] and anorthite [66] as new phases appear at 900 °C.

Figure 8 shows the ^{31}P MAS-NMR of the PWW calcined at different temperatures. The spectra display a peak at about 2.6 ppm. Several reports [70, 71] have shown that this peak indicates the presence of the phosphorus atoms located in one crystallographic site in the fluorapatite phase. After calcination at different temperatures, the spectra did not change from a calcination temperature to another, indicating that the structure of fluorapatite was not altered, which confirm the result of XRD and FTIR.

SEM characterization

The SEM characterization was performed to investigate the microstructure of PWW before and after calcination. The

Table 4 Phases transformation upon thermal treatment

25 °C	600 °C	700 °C	800 °C	900 °C
Carbonate-fluorapatite	Decarbonation	Deacarbonation		
Fluoarpatite			Fluorapatite	Fluorapatite
Calcite	Decarbonation	Decarbonation	Decomposition	
Heulandite K	Decomposition	Decomposition		
Palygorskite	Dehydroxylation	Decomposition		
Gypsum	Dehydroxylation			
Quartz				
	Anhydrite	Anhydrite	Anhydrite	Anhydrite
		Phlogopite	Decomposition	
				Gehlenite
				Anorthite

micrographs show that the PWW has an irregular shape and heterogeneous particles. Figure 9 shows also that the PWW presents small granular crystals, needles and solid deposits. It was clear from the SEM micrographs that the temperature has an effect on the PWW phases. After thermal treatment at different temperatures (600, 700, 800 and 900 °C), the microstructure shows that the particles stay with irregular shape but demonstrate also the appearance and disappearance of some phases by the extinction of needles for example. During the treatment, the SEM shows also the densification of the agglomerates and the formation of glassy phases.

Table 4 summarizes the different phases present in the uncalcined PWW and the phases formed upon the thermal treatment.

Conclusions

The present study was designed to determine the effect of the calcination temperature on the chemical and mineralogical composition of the phosphate washing waste, and the conclusions were:

- The chemical analysis and the XRD pattern of the original PWW have revealed important information: significant amount of silicate, calcium, aluminum and phosphorus are observed. Presence of different phases: heulandite, palygorskite, calcite and carbonate-fluorapatite.
- After calcination, the powder shows significant changes at 800 °C and 900 °C via the total disappearance of calcite, heulandite and palygorskite which generate aluminosilicate and CaO in active state. These two compounds are able to form new phases which can be in this case: phlogopite, C_2S, anorthite and gehlenite.
- The calcined PWW at different temperatures can be a precursor for the synthesis of different materials like zeolite, ceramic and geopolymer.

Acknowledgements The authors would like to acknowledge the both universities for their support. The phosphate washing waste sample was supplied by the Gafsa Phosphate Company "CPG Tunisia"

References

1. Ober JA. Mineral commodity summaries 2018. Report. Reston, VA; 2018.
2. Krekeler MPS, Morton J, Lepp J, Tselepis CM, Samsonov M, Kearns LE. Mineralogical and geochemical investigation of clay-rich mine tailings from a closed phosphate mine, Bartow Florida, USA. Environ Geol. 2007;55(1):123–47. https://doi.org/10.1007/s00254-007-0971-8.
3. Song Q, Li J, Zeng X. Minimizing the increasing solid waste through zero waste strategy. J Clean Prod. 2015;104:199–210. https://doi.org/10.1016/j.jclepro.2014.08.027.
4. Yang Y, Wei Z, Chen Y-L, Li Y, Li X. Utilizing phosphate mine tailings to produce ceramisite. Constr Build Mater. 2017;155:1081–90. https://doi.org/10.1016/j.conbuildmat.2017.08.070.
5. Cánovas CR, Macías F, Pérez-López R, Basallote MD, Millán-Becerro R. Valorization of wastes from the fertilizer industry: current status and future trends. J Clean Prod. 2018;174:678–90. https://doi.org/10.1016/j.jclepro.2017.10.293.
6. Chraiti R, Raddaoui M, Hafiane A. Effluent water quality at phosphate mines in M'Dhilla, Tunisia and its potential environmental effects. Mine Water Environ. 2016;35(4):462–8. https://doi.org/10.1007/s10230-016-0400-x.
7. Marzougui S, Sdiri A, Rekhiss F. Heavy metals' mobility from phosphate washing effluents discharged in the Gafsa area (southwestern Tunisia). Arab J Geosci. 2016. https://doi.org/10.1007/s12517-016-2613-5.
8. Boughzala K, Fattah N, Bouzouita K, Ben Hassine H. Etude minéralogique et chimique du phosphate naturel d'Oum El Khecheb (Gafsa, Tunisie). Revue science des matériaux, Laboratoire LARHYSS. 2015;6:11–29.
9. Gallala W, Saïdi M, el Hajii S, Zayani K, Gaied ME, Montacer M. Characterization and valorization of Tozeur-Nefta phosphate ore deposit (southwestern Tunisia). Procedia Eng. 2016;138:8–18.

10. Galfati I, Sassi AB, Zaier A, Bouchardon JL, Bilal E, Joron J-L, et al. Geochemistry and mineralogy of Paleocene-Eocene Oum El Khecheb phosphorites (Gafsa-Metlaoui Basin) Tunisia. Geochem J. 2010;44(3):189–210.
11. Elgharbi S, Horchani-Naifer K, Ferid M. Investigation of the structural and mineralogical changes of Tunisian phosphorite during calcinations. J Therm Anal Calorim. 2015;119(1):265–71.
12. Galai H, Sliman F. Mineral characterization of the Oum El Khacheb phosphorites (Gafsa-Metlaoui basin; S Tunisia). Arab J Chem. 2014. https://doi.org/10.1016/j.arabjc.2014.10.007.
13. Mekki A, Awali A, Aloui F, Loukil S, Sayadi S. Characterization and toxicity assessment of wastewater from rock phosphate processing in Tunisia. Mine Water Environ. 2017;36(4):502–7.
14. Ahmed AH, Tlili A, Affouri H. ETUDE MINÉRALOGIQUE ET ORGANO-GEOCHIMIQUE DU FACIÈS PHOSPHATÉ YPRESIEN DU SUD OUEST TUNISIEN.
15. Jellali S, Wahab MA, Hassine RB, Hamzaoui AH, Bousselmi L. Adsorption characteristics of phosphorus from aqueous solutions onto phosphate mine wastes. Chem Eng J. 2011;169(1–3):157–65. https://doi.org/10.1016/j.cej.2011.02.076.
16. Jellali S, Wahab MA, Anane M, Riahi K, Bousselmi L. Phosphate mine wastes reuse for phosphorus removal from aqueous solutions under dynamic conditions. J Hazard Mater. 2010;184(1–3):226–33. https://doi.org/10.1016/j.jhazmat.2010.08.026.
17. Hakkou R, Benzaazoua M, Bussière B. Valorization of phosphate waste rocks and sludge from the moroccan phosphate mines: challenges and perspectives. Procedia Eng. 2016;138:110–8. https://doi.org/10.1016/j.proeng.2016.02.068.
18. Zhang P. Comprehensive recovery and sustainable development of phosphate resources. Procedia Eng. 2014;83:37–51. https://doi.org/10.1016/j.proeng.2014.09.010.
19. Baccour H, Koubaa H, Baklouti S (eds). Phosphate sludge from Tunisian phosphate mines: valorisation as ceramics products. In: Euro-mediterranean conference for environmental integration; 2017. Springer.
20. Loutou M, Hajjaji M, Mansori M, Favotto C, Hakkou R. Heated blends of clay and phosphate sludge: microstructure and physical properties. J Asian Ceram Soc. 2018;4(1):11–8. https://doi.org/10.1016/j.jascer.2015.10.003.
21. Chen Q, Zhang Q, Fourie A, Xin C. Utilization of phosphogypsum and phosphate tailings for cemented paste backfill. J Environ Manag. 2017;201:19–27. https://doi.org/10.1016/j.jenvman.2017.06.027.
22. Loutou M, Hajjaji M, Mansori M, Favotto C, Hakkou R. Phosphate sludge: thermal transformation and use as lightweight aggregate material. J Environ Manag. 2013;130:354–60. https://doi.org/10.1016/j.jenvman.2013.09.004.
23. Rashed MN, Mohamed AR, Awadallah MA. Chemically activated phosphate slime as adsorbent for heavy metals removal from polluted water. Int J Environ Waste Manag. 2015;16(2):145–65.
24. Khemakhem M, Khemakhem S, Ayedi S, Amar RB. Study of ceramic ultrafiltration membrane support based on phosphate industry subproduct: application for the cuttlefish conditioning effluents treatment. Ceram Int. 2011;37(8):3617–25. https://doi.org/10.1016/j.ceramint.2011.06.020.
25. Khemakhem M, Khemakhem S, Ayedi S, Cretin M, Ben Amar R. Development of an asymmetric ultrafiltration membrane based on phosphates industry sub-products. Ceram Int. 2015;41(9):10343–8. https://doi.org/10.1016/j.ceramint.2015.05.101.
26. Dabbebi R, Barroso de Aguiar JL, Camões A, Samet B, Baklouti S. Effect of the calcinations temperatures of phosphate washing waste on the structural and mechanical properties of geopolymeric mortar. Constr Build Mater. 2018;185:489–98. https://doi.org/10.1016/j.conbuildmat.2018.07.045.
27. Moukannaa S, Loutou M, Benzaazoua M, Vitola L, Alami J, Hakkou R. Recycling of phosphate mine tailings for the production of geopolymers. J Clean Prod. 2018;185:891–903. https://doi.org/10.1016/j.jclepro.2018.03.094.
28. Liu X, Zhang Y, Liu T, Cai Z, Sun K. Characterization and separation studies of a fine sedimentary phosphate ore slime. Minerals. 2017;7(6):94. https://doi.org/10.3390/min7060094.
29. Claverie M, Martin F, Tardy JP, Cyr M, De Parseval P, Grauby O, et al. Structural and chemical changes in kaolinite caused by flash calcination: formation of spherical particles. Appl Clay Sci. 2015;114:247–55. https://doi.org/10.1016/j.clay.2015.05.031.
30. Chotoli FF, Quarcioni VA, Lima SS, Ferreira JC, Ferreira GM. Clay activation and color modification in reducing calcination process: development in lab and industrial scale. Calcined Clays for Sustainable Concrete. Berlin: Springer; 2015. p. 479–86.
31. Ahmed AH, Tlili A, Affouri H. ETUDE MINÉRALOGIQUE ET ORGANO-GEOCHIMIQUE DU FACIÈS PHOSPHATÉ YPRESIEN DU SUD OUEST TUNISIEN; 2008.
32. Gelves JF, Gallego GS, Marquez MA. Mineralogical characterization of zeolites present on basaltic rocks from Combia geological formation, La Pintada (Colombia). Microporous Mesoporous Mater. 2016;235:9–19. https://doi.org/10.1016/j.micromeso.2016.07.035.
33. Christidis G, Moraetis D, Keheyan E, Akhalbedashvili L, Kekelidze N, Gevorkyan R, et al. Chemical and thermal modification of natural HEU-type zeolitic materials from Armenia, Georgia and Greece. Appl Clay Sci. 2003;24(1–2):79–91.
34. Elgharbi S, Horchani-Naifer K, Férid M. Investigation of the structural and mineralogical changes of Tunisian phosphorite during calcinations. J Therm Anal Calorim. 2014;119(1):265–71. https://doi.org/10.1007/s10973-014-4132-5.
35. Yan W, Liu D, Tan D, Yuan P, Chen M. FTIR spectroscopy study of the structure changes of palygorskite under heating. Spectrochim Acta A Mol Biomol Spectrosc. 2012;97:1052–7. https://doi.org/10.1016/j.saa.2012.07.085.
36. Sreenivasan H, Kinnunen P, Heikkinen E-P, Illikainen M. Thermally treated phlogopite as magnesium-rich precursor for alkali activation purpose. Miner Eng. 2017;113:47–54. https://doi.org/10.1016/j.mineng.2017.08.003.
37. Langner R, Fechtelkord M. Aluminium ordering and clustering in synthetic phlogopite: OH/F influence on the Al-content of phlogopite studied by NMR spectroscopy. Eur J Mineral. 2012;24(5):798–814. https://doi.org/10.1127/0935-1221/2012/0024-2227.
38. Traoré K, Kabré TS, Blanchart P. Gehlenite and anorthite crystallisation from kaolinite and calcite mix. Ceram Int. 2003;29(4):377–83. https://doi.org/10.1016/s0272-8842(02)00148-7.
39. Ptáček P, Opravil T, Šoukal F, Havlica J, Holešinský R. Kinetics and mechanism of formation of gehlenite, Al–Si spinel and anorthite from the mixture of kaolinite and calcite. Solid State Sci. 2013;26:53–8. https://doi.org/10.1016/j.solidstatesciences.2013.09.014.
40. Ostrooumov M, Cappelletti P, de'Gennaro R. Mineralogical study of zeolite from New Mexican deposits (Cuitzeo area, Michoacan, Mexico). Appl Clay Sci. 2012;55:27–35. https://doi.org/10.1016/j.clay.2011.09.011.
41. Frinisrasra N, Srasra E. Effect of heating on palygorskite and acid treated palygorskite properties. Электронная обработка материалов. 2008;44(1):43–9.
42. Alujas A, Fernández R, Quintana R, Scrivener KL, Martirena F. Pozzolanic reactivity of low grade kaolinitic clays: influence of calcination temperature and impact of calcination products on

OPC hydration. Appl Clay Sci. 2015;108:94–101. https://doi.org/10.1016/j.clay.2015.01.028.
43. Antonakos A, Liarokapis E, Leventouri T. Micro-Raman and FTIR studies of synthetic and natural apatites. Biomaterials. 2007;28(19):3043–54. https://doi.org/10.1016/j.biomaterials.2007.02.028.
44. Fernández Carrasco L, Torrens Martín D, Morales L, Martínez Ramírez S. Infrared spectroscopy in the analysis of building and construction materials. Rijeka: InTech; 2012.
45. Ramasamy V, Anand P, Suresh G. Synthesis and characterization of polymer-mediated $CaCO_3$ nanoparticles using limestone: a novel approach. Adv Powder Technol. 2018;29(3):818–34. https://doi.org/10.1016/j.apt.2017.12.023.
46. Bishop JL, Lane MD, Dyar MD, King SJ, Brown AJ, Swayze GA. Spectral properties of Ca-sulfates: gypsum, bassanite, and anhydrite. Am Miner. 2014;99(10):2105–15. https://doi.org/10.2138/am-2014-4756.
47. Yin Y, Yin J, Zhang W, Tian H, Hu Z, Ruan M, et al. FT-IR and micro-Raman spectroscopic characterization of minerals in high-calcium coal ashes. J Energy Inst. 2018;91(3):389–96. https://doi.org/10.1016/j.joei.2017.02.003.
48. Xavier KCM, Santos MSF, Osajima JA, Luz AB, Fonseca MG, Silva Filho EC. Thermally activated palygorskites as agents to clarify soybean oil. Appl Clay Sci. 2016;119:338–47. https://doi.org/10.1016/j.clay.2015.10.037.
49. Burzo E. Heulandite and stilbite groups of tectosilicates. In: Wijn HPJ, editor. Datasheet from Landolt-Börnstein—Group III condensed matter: "Tectosilicates" in SpringerMaterials, vol. 27I6γ. Berlin: Springer; 2013. https://doi.org/10.1007/978-3-642-30612-9_2.
50. Chmielarz L, Kowalczyk A, Michalik M, Dudek B, Piwowarska Z, Matusiewicz A. Acid-activated vermiculites and phlogophites as catalysts for the DeNOx process. Appl Clay Sci. 2010;49(3):156–62. https://doi.org/10.1016/j.clay.2010.04.020.
51. Pan X, Zhang D, Wu Y, Yu H. Synthesis and characterization of calcium aluminate compounds from gehlenite by high-temperature solid-state reaction. Ceram Int. 2018;44(12):13544–50. https://doi.org/10.1016/j.ceramint.2018.04.186.
52. Shi T, Gao Y, Corr DJ, Shah SP. FTIR study on early-age hydration of carbon nanotubes-modified cement-based materials. Adv Cem Res. 2018. https://doi.org/10.1680/jadcr.16.00167.
53. Maheswaran S, Kalaiselvam S, Saravana Karthikeyan SKS, Kokila C, Palani GS. β-Belite cements (β-dicalcium silicate) obtained from calcined lime sludge and silica fume. Cem Concr Compos. 2016;66:57–65. https://doi.org/10.1016/j.cemconcomp.2015.11.008.
54. Daghmehchi M, Rathossi C, Omrani H, Emami M, Rahbar M. Mineralogical and thermal analyses of the Hellenistic ceramics from Laodicea Temple, Cement. Appl Clay Sci. 2018;162:146–54. https://doi.org/10.1016/j.clay.2018.06.007.
55. Sharma SK, Simons B, Yoder H. Raman study of anorthite, calcium Tschermak's pyroxene, and gehlenite in crystalline and glassy states. Am Miner. 1983;68(11–12):1113–25.
56. Wijn H. Tectosilicates. Landolt Börnstein; 2011(27).
57. Smith M, Mackenzie K. Multinuclear solid state NMR of inorganic materials. Pergamon Materials Series. New York: Elsevier; 2002.
58. Ashbrook SE, Dawson DM. NMR spectroscopy of minerals and allied materials. Nuclear Magn Reson. 2016;45:1.
59. Rhouta B, Zatile E, Bouna L, Lakbita O, Maury F, Daoudi L, et al. Comprehensive physicochemical study of dioctahedral palygorskite-rich clay from Marrakech High Atlas (Morocco). Phys Chem Miner. 2013;40(5):411–24. https://doi.org/10.1007/s00269-013-0579-3.
60. Lippmaa E, Maegi M, Samoson A, Tarmak M, Engelhardt G. Investigation of the structure of zeolites by solid-state high-resolution silicon-29 NMR spectroscopy. J Am Chem Soc. 1981;103(17):4992–6.
61. Fang Y, Chang J. Rapid hardening β-C2S mineral and microstructure changes activated by accelerated carbonation curing. J Therm Anal Calorim. 2017;129(2):681–9. https://doi.org/10.1007/s10973-017-6165-z.
62. Sánchez-Herrero MJ, Fernández-Jiménez A, Palomo Á, Klein L. Alkaline hydration of C_2S and C_3S. J Am Ceram Soc. 2016;99(2):604–11. https://doi.org/10.1111/jace.13985.
63. Walkley B, San Nicolas R, Sani M-A, Bernal SA, van Deventer JSJ, Provis JL. Structural evolution of synthetic alkali-activated $CaO–MgO–Na_2O–Al_2O_3–SiO_2$ materials is influenced by Mg content. Cem Concr Res. 2017;99:155–71. https://doi.org/10.1016/j.cemconres.2017.05.006.
64. Florian P, Veron E, Green TFG, Yates JR, Massiot D. Elucidation of the Al/Si ordering in gehlenite $Ca_2Al_2SiO_7$ by combined 29Si and 27Al NMR spectroscopy/quantum chemical calculations. Chem Mater. 2012;24(21):4068–79. https://doi.org/10.1021/cm3016935.
65. Lee NK, Koh KT, An GH, Ryu GS. Influence of binder composition on the gel structure in alkali activated fly ash/slag pastes exposed to elevated temperatures. Ceram Int. 2017;43(2):2471–80. https://doi.org/10.1016/j.ceramint.2016.11.042.
66. Allu AR, Balaji S, Tulyaganov DU, Mather GC, Margit F, Pascual MJ, et al. Understanding the formation of $CaAl_2Si_2O_8$ in melilite-based glass-ceramics: combined diffraction and spectroscopic studies. ACS Omega. 2017;2(9):6233–43. https://doi.org/10.1021/acsomega.7b00598.
67. Brus J, Abbrent S, Kobera L, Urbanova M, Cuba P. Advances in 27Al MAS NMR studies of geopolymers. Annu Rep NMR Spectrosc. 2016;88:79–147. https://doi.org/10.1016/bs.arnmr.2015.11.001.
68. Rusmin R, Sarkar B, Biswas B, Churchman J, Liu Y, Naidu R. Structural, electrokinetic and surface properties of activated palygorskite for environmental application. Appl Clay Sci. 2016;134:95–102. https://doi.org/10.1016/j.clay.2016.07.012.
69. Mozgawa W, Fojud Z, Handke M, Jurga S. MAS NMR and FTIR spectra of framework aluminosilicates. J Mol Struct. 2002;614(1–3):281–7.
70. Ayadi I, Ayed FB. Mechanical optimization of the composite biomaterial based on the tricalcium phosphate, titania and magnesium fluoride. J Mech Behav Biomed Mater. 2016;60:568–80. https://doi.org/10.1016/j.jmbbm.2016.03.020.
71. Ayed FB, Bouaziz J. Sintering of tricalcium phosphate–fluorapatite composites by addition of alumina. Ceram Int. 2008;34(8):1885–92. https://doi.org/10.1016/j.ceramint.2007.07.017.